



HAL
open science

Hydrogeophysical characterization and determination of petrophysical parameters by integrating geophysical and hydrogeological data at the limestone vadose zone of the Beauce aquifer

Mohamad Abbas, Jacques Deparis, Arnaud Isch, Céline Mallet, Clara Jodry, Mohamed Azaroual, Bouamama Abbar, Jean-Michel Baltassat

► To cite this version:

Mohamad Abbas, Jacques Deparis, Arnaud Isch, Céline Mallet, Clara Jodry, et al.. Hydrogeophysical characterization and determination of petrophysical parameters by integrating geophysical and hydrogeological data at the limestone vadose zone of the Beauce aquifer. *Journal of Hydrology*, 2022, pp.128725. 10.1016/j.jhydrol.2022.128725 . hal-03864896

HAL Id: hal-03864896

<https://brgm.hal.science/hal-03864896v1>

Submitted on 22 Nov 2022

HAL is a multi-disciplinary open access archive for the deposit and dissemination of scientific research documents, whether they are published or not. The documents may come from teaching and research institutions in France or abroad, or from public or private research centers.

L'archive ouverte pluridisciplinaire **HAL**, est destinée au dépôt et à la diffusion de documents scientifiques de niveau recherche, publiés ou non, émanant des établissements d'enseignement et de recherche français ou étrangers, des laboratoires publics ou privés.

Journal Pre-proofs

Research papers

Hydrogeophysical characterization and determination of petrophysical parameters by integrating geophysical and hydrogeological data at the limestone vadose zone of the Beauce aquifer

M. Abbas, J. Deparis, A. Isch, C. Mallet, C. Jodry, M. Azaroual, B. Abbar, J.M. Baltassat

PII: S0022-1694(22)01295-1
DOI: <https://doi.org/10.1016/j.jhydrol.2022.128725>
Reference: HYDROL 128725

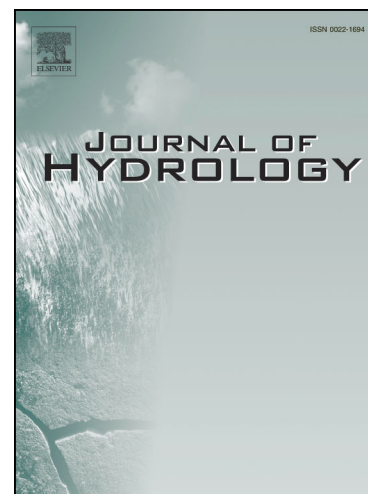
To appear in: *Journal of Hydrology*

Received Date: 15 February 2022
Revised Date: 10 October 2022
Accepted Date: 11 October 2022

Please cite this article as: Abbas, M., Deparis, J., Isch, A., Mallet, C., Jodry, C., Azaroual, M., Abbar, B., Baltassat, J.M., Hydrogeophysical characterization and determination of petrophysical parameters by integrating geophysical and hydrogeological data at the limestone vadose zone of the Beauce aquifer, *Journal of Hydrology* (2022), doi: <https://doi.org/10.1016/j.jhydrol.2022.128725>

This is a PDF file of an article that has undergone enhancements after acceptance, such as the addition of a cover page and metadata, and formatting for readability, but it is not yet the definitive version of record. This version will undergo additional copyediting, typesetting and review before it is published in its final form, but we are providing this version to give early visibility of the article. Please note that, during the production process, errors may be discovered which could affect the content, and all legal disclaimers that apply to the journal pertain.

© 2022 Published by Elsevier B.V.



1 **Hydrogeophysical characterization and determination of petrophysical parameters by integrating**
2 **geophysical and hydrogeological data at the limestone vadose zone of the Beauce aquifer**

3 M. Abbas¹ *, J. Deparis², A. Isch¹, C. Mallet¹, C. Jodry³, M. Azaroual^{1,2}, B. Abbar¹, and J. M.
4 Baltassat²

5 ¹ Univ. Orléans, CNRS, BRGM, ISTO, UMR 7327, F-45071, Orléans, France.

6 ² BRGM, French Geological Survey, 45060 Orléans, France.

7 ³ UNISTRA, Azerbaijan State Oil and Industry University, French Azerbaijani University,
8 Baku, Azerbaijan.

9

10 *Corresponding Author (abbas_mohammad@live.com)

11

12

13

14

15

16

17

18

19

20

21

22

23

24

25

26

27

28

29

30

31 Abstract

32 The hydrological characterization of the vadose zone remains a major challenge considering
33 the spatiotemporal variability of its properties and the limitations associated with hydrological
34 measurements techniques. Geophysical methods, in particular the DC-resistivity and ground
35 penetrating radar, can provide large scale images of hydrogeological structures and a non-
36 invasive assessment of the subsurface dynamic processes. However, these approaches rely on
37 the accuracy of the petrophysical relationships connecting the geophysical parameters to
38 hydrogeological ones, where the site-specific determination of the associated petrophysical
39 parameters is considered crucial. The first objective of this study was to investigate the
40 relationship between the water content, geological properties, and geophysical attributes at the
41 vadose zone of a vulnerable limestone aquifer. The second objective aimed to obtain the
42 Archie's and Complex Refractive Index Model (CRIM) petrophysical parameters by using
43 borehole electrical resistivity and cross-hole ground penetrating radar data. For this purpose,
44 we adopted a grid search inversion algorithm where the field geophysical data were integrated
45 with water content profiles simulated by using HYDRUS-1D. The vadose zone profile was
46 divided into three layers, and the inversion was carried out for the petrophysical parameters in
47 each of the model layers. The electrical resistivity and relative dielectric permittivity data
48 showed a very good correspondence with the simulated and experimental water content
49 distributions along the vadose zone profile. The petrophysical parameters estimated by the
50 inversion showed values that fall in the ranges reported in the literature. Similar values have
51 been observed in the different model layers, with slight differences that were attributed to the
52 vertical heterogeneities associated with the alteration and fracturation features of the limestone
53 vadose zone. This study showed a very good correlation between geophysical, hydrogeological
54 and geological data, and highlighted the presence of heterogeneities that can have profound
55 effects on the vadose zone water dynamics.

56 **Key Words:** Electrical Resistivity, Ground Penetrating Radar, Archie, Complex Refractive
57 Index Model, Water Content.

58 **1. Introduction**

59 Improved understanding of water flow and transport processes in the vadose zone (VZ) is
60 crucial, considering the critical role this compartment of the subsurface plays within the
61 biosphere and in the transmission of water and contaminants from the surface to the
62 groundwater. Contamination sources mainly originate in the VZ where the transfer of
63 contaminants is impacted by the medium heterogeneities (e.g., fractures, induced preferential
64 flow and rapid infiltration), and by interactions involving a complex interplay between coupled
65 physical, geochemical, and microbial processes (Arora et al., 2019; Stephens, 2019; Nimmo,
66 2005). Therefore, a better knowledge of the hydrogeological processes and water content
67 distribution within the VZ is essential to protect groundwater resources.

68 Conventionally, water content measurements were carried out by single-point techniques, such
69 as time domain reflectometry (TDR) or neutron probes (He et al., 2021; Isch et al., 2019;
70 Skierucha et al., 2012; Evett, 2008; Verhoef et al., 2006; Evett, 2003). Advancements in these
71 techniques (e.g., multi-TDR systems) provided the possibility of time-lapse water content
72 monitoring and eventual preferential flow paths detection (Herkelrath et al., 1991). However,
73 such measurements are intrusive, limited to very shallow depths, and provide restricted
74 information at only a series of point locations. These measurements are often not representative
75 of the field scale spatial water content distribution (Robinson et al., 2003). The difficulties
76 involved in obtaining 2-D or 3-D hydrologic images by exploiting such sparse local data
77 introduced geophysical methods as alternative ways of monitoring water content distribution
78 and water fluxes within the VZ (Binley et al., 2015; Vereecken et al., 2006; Rubin and Hubbard,
79 2005).

80 Geophysical methods have shown a great potential in providing large-scale and high spatial
81 resolution images of the subsurface hydrogeological processes (Binley et al., 2015; 2010).
82 Several surface and cross-borehole geophysical methods have been recently used for different
83 hydrological applications. These methods include the ground penetrating radar (GPR) (Dafflon
84 et al., 2011; Lunt et al., 2005; Binley et al., 2001), seismic techniques (Blazevic et al., 2020),
85 electrical resistivity (ER) (Mallet et al., 2021; Johnson et al., 2015; Robinson et al., 2008), self-
86 potential (Abbas et al, 2017; Ahmed et al., 2014; Jardani et al., 2012), induced polarization
87 (Johnson et al., 2010) and nuclear magnetic resonance (Vilhelmsen et al., 2014). Additionally,
88 geophysical methods have been recently used to characterize and quantify processes and
89 interactions in the soil–rhizosphere–atmosphere agricultural ecosystem continuum (Garré et al.,
90 2021).

91 In particular, the GPR and ER methods have been frequently used to investigate water flow
92 dynamics and identify hydrodynamic parameters (Klotzsche et al., 2019, 2018; Paz et al., 2017;
93 Binley et al., 2015). Thanks to well-established petrophysical relationships between water
94 content and both electrical resistivity (e.g., Archie, 1942) and dielectric permittivity (e.g., Topp
95 et al., 1980) of porous media, these methods can provide valuable information on water flow
96 that can be used to parameterize and constrain hydrogeological models. Relative variations of
97 water content distribution in VZ profiles have been successfully estimated by GPR and ER data.
98 These observations were used to monitor infiltration experiments and visualize flow patterns,
99 quantify petrophysical parameters, characterize preferential flow pathways in fractured media
100 (De Jong et al., 2020; Gance et al., 2016; Wehrer and Slater, 2015; Klotzsche et al., 2013;
101 Steelman and Endres, 2011; Brunet et al., 2010; Cassiani et al., 2009b ; Looms et al., 2008;
102 Linde et al., 2006; Kowalsky et al., 2005; Huisman et al., 2003; Binley et al., 2002a; Hubbard
103 et al., 2001a), and even assess the variations of the soil water content associated with root water
104 uptake (Mary et al., 2018; Hagrey, 2007).

105 Generally, the water content estimates derived from GPR and ER data showed high accuracy
106 and a good reproducibility. However, geophysical methods cannot directly provide water
107 content values. This approach is dependent on the empirical relationships between the sensed
108 physical parameters and the subsurface parameters of interest (e.g., porosity and water
109 saturation), especially in complex heterogeneous mediums such as carbonate environments,
110 which are often characterized by a complex multiple-porosity system consisting of matrix
111 porosity and fissures, vugs, fractures and karst networks (Mallet et al., 2022; Aldana et al.,
112 2021; Ammar and Kamal, 2017; Mount and Comas, 2014 ; Lucia, 2007). Difficulties arise in
113 the need of time-consuming and expensive laboratory calibration of the petrophysical
114 relationships that are basically suitable only for homogeneous formations, and influenced by
115 properties such as the porosity and tortuosity patterns of the medium under study (Mohamed
116 and Hamada, 2017; Glover, 2016). Estimating parameters such as the water content and
117 porosity from geophysical data by using documented literature values of petrophysical
118 parameters can induce a lot of uncertainties in the absence of site-specific calibration.
119 Achieving an efficient determination of site-specific petrophysical parameters is expected to
120 reduce such uncertainties, and can provide a large-scale and time-saving estimation of water
121 content by avoiding destructive and time-consuming hydrogeological measurements and
122 laboratory calibrations.

123 The presented study is carried out within the framework of the “Observatory of Transfers in the
124 Vadose Zone” (O-ZNS) platform. The general objective of the O-ZNS platform is to investigate
125 the water-rock-biosphere interactions and their associated mass and heat transfer processes in
126 the VZ. This can provide a better understanding of the VZ dynamics and coupled processes by
127 providing physical, biogeochemical and spatially resolved hydrodynamic parameters capable
128 of characterizing water flow patterns and parameterizing transport models. This study first
129 investigates the relationship between geophysical attributes, water content and geological

130 heterogeneities at the vadose zone of a vulnerable limestone aquifer. An inversion algorithm is
131 then used to obtain the Archie's and CRIM's petrophysical parameters by integrating borehole
132 electrical resistivity and cross-hole ground penetrating radar data with water content profiles
133 simulated by HYDRUS-1D.

134 **2. Study site**

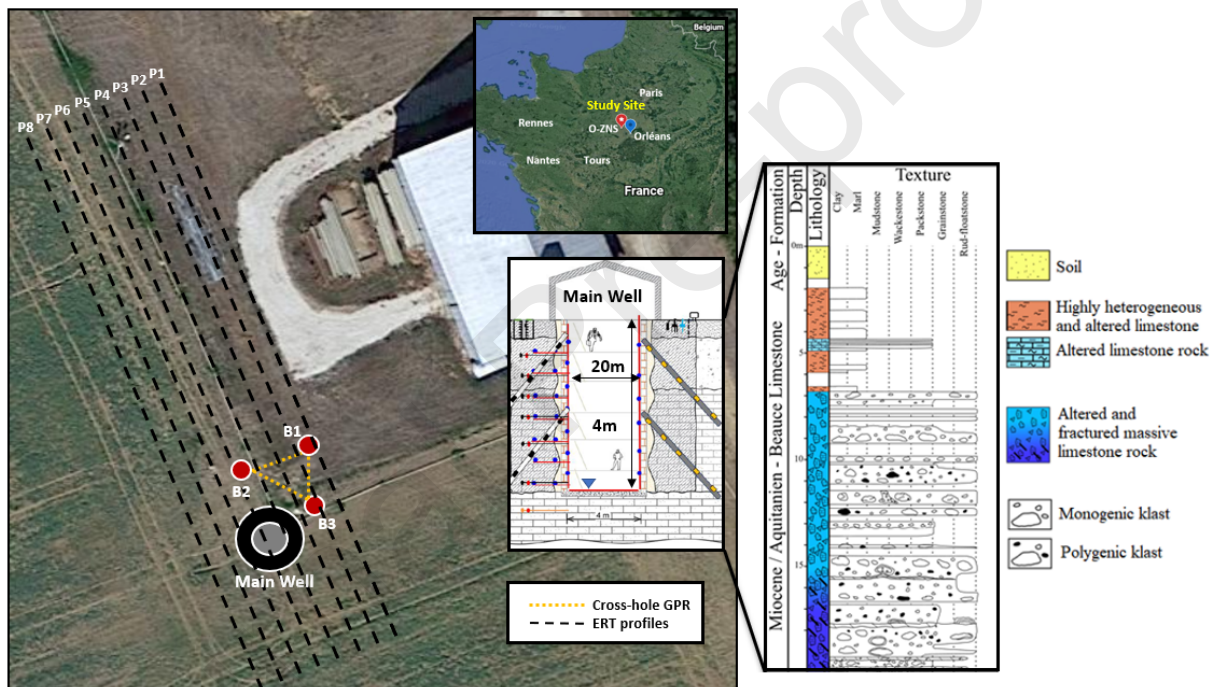
135 **2.1. Description**

136 This study was carried out at the O-ZNS observatory, located in the vicinity of the Beauce
137 limestone aquifer at an agricultural site in Villamblain, France (Fig. 1) (DMS coordinates: $X =$
138 $48^{\circ}1'5.131''$; $Y = 1^{\circ}34'55.333''$). The observatory offers a unique experimental setup, composed
139 of an exceptional well having a depth of 20 m and a diameter of 4 m, along with a number of
140 instrumented boreholes and piezometers. Additionally, the observatory will be equipped with
141 innovative complementary environmental sensors such as fiber-optic sensors (e.g., distributed
142 acoustic sensing, distributed temperature sensing), water content monitoring probes (e.g.,
143 TDR), and samplers. These sensors can provide quantitative measurements relative to fluid and
144 heat transfer processes within the VZ. During its exploitation, which is planned for several
145 decades, the observatory will allow acquiring original and unique data on the mass (water,
146 solutes, organic and inorganic contaminants, gases, etc.) and heat (induced by temperature
147 gradients, microbiological reactions, etc.) transfer processes across the continuum "Soil-VZ-
148 Capillary Fringe -Aquifer" for environmental issues and water management. A detailed
149 description of the observatory instrumentation setup can be found in Abbar et al. (2021).

150 **2.2. Geology**

151 Direct observations of undisturbed cores complemented with optical log imagery revealed
152 significant vertical and lateral lithological heterogeneities within the VZ units. Three main
153 lithological units have been identified by the direct core observations (Fig. 1): (1) A first top

154 soil unit having a thickness ranging between 0.9 and 1.8 m, and a silt loam texture referred to
 155 as a Hypereutric Cambisol (IUSS Working Group WRB, 2015); (2) a second unit characterized
 156 by highly heterogeneous and altered (i.e., fractures, weathering, oxidation) incoherent
 157 limestone facies reaching a depth of around 7 m; and (3) a third unit of hard limestone rock
 158 (Pithiviers limestone) extending from a depth of around 7 m down to 20 m with a clear evolution
 159 of alteration, fracturation and karstification with depth. The water table had an average depth
 160 ranging between 16.5 m and 20.5 m over the last decade, with observed historical variations
 161 ranging between 14.5 m and 22.5 m since 1966 (Isch et al., 2022).



162
 163 **Fig. 1.** Study site location, instrumentation, geology and geophysical measurements setup. The
 164 figure only shows the boreholes used for this study, several other boreholes surrounding the
 165 main well are present at the study site.

166 3. Methods

167 3.1. Geophysical data acquisition

168 The O-ZNS infrastructure allows the combination of different geophysical methods and focuses
169 on integrating borehole, cross-hole and surface geophysical techniques that are sensitive to
170 transfer and flow processes. In this section, we present the acquisition protocols of the electrical
171 resistivity tomography (ERT), borehole ER and cross-hole GPR data used in this study.

172 **3.1.1. Electrical Resistivity**

173 A total of 8 ERT profiles were acquired on the 18th of April, 2019 by using a Syscal-Pro 96
174 resistivity meter (Iris Instruments, France) connected to a Syscal Switch Pro 96. The profiles
175 had 48 electrodes each, with an inter-profile spacing of 5 m (Fig. 1). A 2.5 m electrodes spacing
176 was chosen in order to ensure both, an acceptable resolution, and a maximum investigation
177 depth of about 23 m. The measurements were acquired in Dipole-Dipole and Wenner-
178 Schlumberger configurations. Basic filtering steps have been conducted on the acquired ERT
179 profiles (e.g., exterminating bad data points). The profiles were then inverted by Res2Dinv
180 (Loke and Barker,1996) that uses a smoothness-constrained Gauss-Newton least-squares
181 inversion technique to obtain a 2D electrical resistivity model of the subsurface from the field
182 apparent resistivity data (Griffiths and Barker, 1993). The result is a 2D smoothness-constrained
183 distribution of electrical resistivity in the VZ. The effect of temperature variations was
184 considered negligible on the electrical resistivity data along the first 20 meters of the subsurface.
185 This was assumed due to the observed low variations of temperature as a function of depth in
186 the VZ at this time of the year.

187 On the other hand, the ER borehole data were obtained from three different boreholes logs (B1,
188 B2 and B3, cf. Fig. 1) on the 23rd of March, 2017 by means of the dual induction-laterolog
189 (DIL) method. This method consists of focused electrical measurements that rely on transmitter
190 and receiver coils. The measurements are based on an alternating current that generate eddy
191 currents which in turn produce a secondary electromagnetic field. The latter induces an
192 alternating voltage proportional to the formation electrical conductivity in the receiver coil. The

193 transmitter-receiver pair which uses a low frequency is designed to minimize the effects of the
 194 borehole and optimize the depth of investigation and the measurement vertical resolution. A
 195 measurement point spacing of 2 cm was used, with a maximum penetration depth varying
 196 between 18 m and 19 m depending on each of the borehole's maximum accessible depth.

197 **3.1.2. Ground Penetrating Radar**

198 The cross-hole GPR measurements were acquired by using a ProEx GPR system (Malå
 199 Geosciences) on the 24th of January, 2019. The measurements were done by using 100 MHz
 200 borehole antennae with a sampling frequency of 1000 MHz and a measurement period of
 201 240 ns. Zero offset profiles (ZOP) were acquired between the three boreholes B1, B2 and B3
 202 (TXB2_RXB1, TXB1_RXB3 and TXB2_RXB3) (Fig. 1). The ZOP method is a commonly
 203 used approach for borehole GPR acquisition surveys (Klotzsche et al., 2019). Throughout the
 204 ZOP measurements, the transmitting (Tx) and receiving (Rx) antennas are moved
 205 simultaneously in two different boreholes with a fixed step size. To conduct the ZOP
 206 measurements, the antenna were first pushed to the bottom of each of the boreholes where the
 207 maximum accessible depth was 18.98 m (water table). The antennae were then pulled
 208 simultaneously towards the surface by using a 0.5 m fixed step size.

209 One-dimensional velocity profiles were then determined by a standard ray-based analysis
 210 approach. For simplicity, the medium was assumed to have no horizontal variation of velocity
 211 while obtaining the one-dimensional velocity profiles. After picking the first arrivals (in
 212 ReflexW©), the arrival time (t) and the distance between the boreholes were used to determine
 213 the GPR electromagnetic wave velocity (v) through the following equation:

$$v = \left(\frac{d}{t - T_0} \right), \quad (1)$$

214 where T_0 is the time-zero offset, which was obtained by conducting multi-offset measurements
 215 with the antenna in free-space. In low-loss and non-magnetic material such as carbonate

216 formations (e.g., limestone), the relative dielectric permittivity (ϵ_r) can be then determined at
217 different depths by using the following equation:

$$\epsilon_r = (c/v)^2, \quad (2)$$

218 where c is the velocity of an electromagnetic wave in vacuum (~ 0.3 m/ns). Relative dielectric
219 permittivity profiles were then determined from the obtained velocity profiles by using Eq. 2.

220 **3.2. Hydraulic properties measurements and simulation of water flow within the VZ**

221 **3.2.1. Hydraulic properties of the vadose zone samples**

222 Fifteen undisturbed samples representative of the VZ (0-20 m deep) were chosen according to
223 the lithological observations made from the three cored boreholes B1, B2 and B3 (Isch et al.,
224 2022). The samples included three soil samples (S_A , S_B and S_C), four soft sediments and
225 powdery limestone samples (P_A , P_B , P_C and P_D), two calcareous sand samples (I_A and I_B), and
226 six limestone rock samples (R_A , R_B , R_C , R_D , R_E and R_F). These samples were used to estimate
227 the water retention $\theta(h)$ and hydraulic conductivity $K(h)$ curves by applying the multistep
228 outflow method (Aldana et al., 2021). The multistep outflow experiments were conducted by
229 using a triaxial system based on the experimental procedure described by Eching et al. (1994).
230 The hydraulic conductivity was calculated from the outflow data based on the method described
231 by Gardner (1956).

232 **3.2.2. Simulation of water flow in the vadose zone**

233 Simulation of water flow within the VZ was then performed over a 55 years period (1966-2020)
234 on a 23 m deep VZ profile (borehole B2) composed of fifteen layers and reconstituted with the
235 HYDRUS-1D software (Šimůnek et al., 2016). The simulation of water flow was based on the
236 one-dimensional vertical water flow in the VZ described by Richards equation (Richards,
237 1931):

$$\frac{\partial \theta}{\partial t} = \frac{\partial}{\partial z} \left[K \left(\frac{\partial h}{\partial z} + 1 \right) \right] - S, \quad (3)$$

238 where θ is the volumetric water content (cm^3/cm^3), z is the coordinate along the vertical axis
 239 (cm), t is the time, h is the matric head (cm), K is the hydraulic conductivity (cm/d) and S is a
 240 sink-source term. The Mualem-Van Genuchten analytical model (MVG) was used for the
 241 description of the VZ hydraulic properties. The van Genuchten's expression (van Genuchten,
 242 1980) was used to describe the water retention curve:

$$\theta(h) = \begin{cases} \theta_r + \frac{\theta_s - \theta_r}{[1 + |\alpha h|^n]^m} & h < 0 \\ \theta_s & h \geq 0 \end{cases} \quad (4)$$

$$\text{with} \quad m = 1 - \frac{1}{n} \quad n > 1,$$

243 where θ_r and θ_s are the residual and saturated volumetric water content (cm^3/cm^3) respectively.
 244 α is an empirical parameter related to the matric head (cm^{-1}), and n is a pore size distribution
 245 parameter (-). The statistical pore connection model of Mualem (1976) was then used to predict
 246 the hydraulic conductivity from the water retention curve:

$$K(h) = K_s S_e^l \left[1 - \left(1 - S_e^{\frac{1}{m}} \right)^m \right]^2 \quad (5)$$

$$\text{with} \quad S_e = \frac{\theta - \theta_r}{\theta_s - \theta_r},$$

247 where K_s is the saturated hydraulic conductivity (cm/d), S_e is the effective saturation (-) and l
 248 is a pore connectivity parameter (-) fixed at the value of 0.5 (Mualem, 1976). The measured
 249 water retention and hydraulic conductivity data were fitted to the $\theta(h)$ and $K(h)$ curves with the
 250 MVG model (Eq. 4 and Eq. 5) by using the RETC software (van Genuchten et al., 1991) to
 251 infer the VZ hydraulic properties used in our simulations. The representation of the VZ profile

252 for B2, the values of experimental and fitted (with RETC) saturated volumetric water content
 253 (θ_s) and fitted hydraulic conductivity (K_s , in cm/d) are given in Table 1. Water table level and
 254 meteorological data were collected from monitoring stations located at the villages of Poiseaux
 255 (4 km from the study site) and Bricy (20 km from the study site) respectively. While the weather
 256 conditions at the study site may differ slightly during intense and localized rainy events relative
 257 to those observed at the Bricy station, these are however considered to be representative over a
 258 period of more than 50 years.

259 **Table 1.** (a) Description of the samples considered for the representation of the VZ profile and
 260 the simulation of water flow with HYDRUS-1D: depth, description, saturated water content (θ_s
 261), experimental saturated water content ($\theta_{sExp.}$), hydraulic conductivity (K_s), α , and n .

Geological Unit	Depth (m)	Sample	Description	θ_s (cm ³ /cm ³)	$\theta_{sExp.}$ (cm ³ /cm ³)	K_s (cm/d)	α cm ⁻¹	n (/)
1	0.00-0.30	S _A	Soil	0.4735	0.4864	30.24	0.0242	1.15
	0.31-0.60	S _B	Soil	0.4661	0.4612	53.57	0.0242	1.16
	0.61-0.90	S _C	Soil	0.5002	0.4162	47.52	0.0366	1.16
2	0.91-1.30	P _A	Powdery limestone	0.4511	0.4230	7.31	0.0247	1.17
	1.30-3.50	P _B	Powdery limestone	0.3659	0.3525	0.455	0.0073	1.25
	3.51-4.10	I _A	Calcareous sand	0.3918	0.3775	35.22	0.0715	1.20
	4.11-4.60	P _C	Powdery limestone	0.2969	0.3080	0.143	0.0031	1.22
	4.61-4.90	I _B	Calcareous sand	0.3698	0.4336	285.49	0.1600	1.23
	4.91-5.20	R _A	Altered rock	0.2984	0.3400	5000	0.5156	1.36
	5.21-5.50	I _B	Calcareous sand	0.3698	0.4336	285.49	0.1600	1.23
	5.51-6.60	P _D	Powdery limestone	0.3527	0.3491	0.185	0.0040	1.22
3	6.61-9.00	R _B	Massive rock	0.1547	0.1499	1.32	0.0150	1.16
	9.01-11.20	R _D	Massive rock	0.0949	0.1180	0.402	0.0096	1.17
	11.21-11.40	R _C	Massive rock	0.0504	0.0491	0.0097	0.0014	1.23
	11.41-14.00	R _D	Massive rock	0.0949	0.1180	0.402	0.0096	1.17

14.01-16.00	R _E	Massive rock	0.1172	0.1333	500	0.1266	1.15
16.01-19.00	R _F	Massive rock	0.1452	0.1639	500	0.1371	1.19

262

263 4. Petrophysical Modeling

264 4.1. Relative Permittivity

265 The CRIM is a three-phase dielectric mixing model commonly used to describe the relationship
 266 between relative dielectric permittivity and subsurface properties such as water content and
 267 porosity (Huisman et., 2003; West et al., 2001; Roth et al., 1990):

$$\varepsilon_r^\alpha = \phi S_w \varepsilon_w^\alpha + (1 - \phi) \varepsilon_s^\alpha + \phi(1 - S_w) \varepsilon_a^\alpha, \quad (6)$$

268 where ϕ and S_w are the porosity and water saturation respectively, ε_a is the relative dielectric
 269 permittivity of air (given a value of 1), ε_w is the relative dielectric permittivity of water, ε_s is
 270 the relative dielectric permittivity of the solid phase, considered as a source of uncertainty to be
 271 accounted for when using the CRIM.

272 Besides the ε_s , the second source of uncertainty to be accounted for is the factor α which
 273 describes the orientation of the electrical field with respect to the geological
 274 formations' geometry (West et al., 2003; Chan and Knight, 1999; Knoll, 1996; Roth et al., 1990;
 275 Birchak et al., 1974).

276 4.2. Electrical Resistivity

277 In geological formations characterized by medium to coarse grained sediments, the grain
 278 surface conductivity effect can be neglected and the bulk electrical resistivity (ρ_0) can be
 279 related to subsurface properties such as porosity and fluid saturation by the following modified
 280 form of Archie's equation (Winsauer et al., 1952 ; Archie, 1942):

$$\rho_0 = a\rho_f\phi^{-m}S_w^{-n}, \quad (7)$$

281 where ρ_f is the fluid or pore water electrical resistivity, a is an empirical constant originally
282 referred to as the tortuosity or lithology constant (Winsauer et al., 1952), m is the cementation
283 exponent which is considered to be influenced by the degree of cementation of the rock fabric
284 (Glover, 2010; 2009), and n is the saturation exponent which is independent of the rock matrix
285 and describes how the pore water is connected (Glover, 2017; Looms et al., 2008a; Hendrickx
286 et al., 2002).

287 Even though Archie's law does not take the surface conduction into account, it is considered to
288 be applicable if the pore fluid conductivity is largely greater than the surface conduction,
289 especially in the case of low clay content formations such as the limestone rock described within
290 the VZ of our study site (Fig. 1). The need of including the surface conductivity arises when
291 other conducting phases such as clay minerals are present in the rock formation. Therefore,
292 during this study, we applied our approach to the limestone rock facies located at a depth
293 between 6.61 m and 19 m, where geological and mineralogical studies (Aldana et al., 2021)
294 suggested that the surface conduction can be practically neglected.

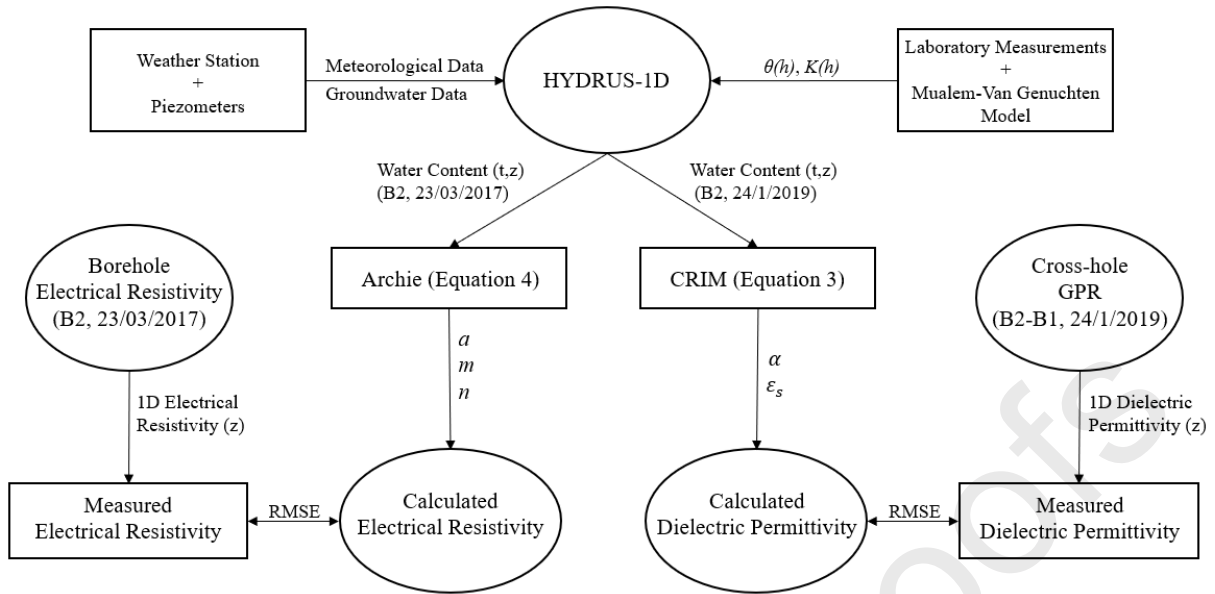
295 4.3. Inversion

296 This study aims to estimate the Archie's and CRIM's parameters that can vary according to the
297 study site conditions, and that are considered as sources of uncertainties in the application of
298 these models for the estimation of water content variations. The numerical approach used in
299 this study is based on a grid search inversion algorithm (Fig. 2). The inversion workflow is
300 based on testing the possible combinations of the petrophysical parameters that can provide the
301 best fit between the measured and simulated data. The estimated data are the electrical
302 resistivity and relative dielectric permittivity values calculated by using the Archie's and
303 CRIM's equations respectively. The ER measured data are the 1D electrical resistivity data

304 acquired by the borehole's ER measurements, while the dielectric permittivity measured data
 305 are those generated from the 1D velocity profiles obtained from the GPR cross-hole
 306 measurements. The fit between the measured and calculated data is evaluated through
 307 calculating the corresponding root mean square error (RMSE) while the algorithm varies the
 308 Archie's (a and m) and CRIM's (α and ϵ_s) petrophysical parameters to be estimated:

$$\text{RMSE} = \sqrt{\frac{\sum_{i=1}^N (x_i - \hat{x}_i)^2}{N}}, \quad (8)$$

309 where x_i represents the observed data, \hat{x}_i represents the data estimated by the model and N is
 310 the total number of data points. The procedure is done separately for the Archie's and CRIM's
 311 models. The water content profiles data used to calculate the dielectric permittivity and
 312 electrical resistivity in the CRIM's and Archie's equation are those simulated by HYDRUS-1D
 313 software. The geophysical data, water content and porosity data used for both models are
 314 obtained from the geophysical measurements and hydrogeological model of borehole B2. The
 315 fluid resistivity in the Archie's equation is given a value of 510 $\mu\text{S}/\text{cm}$ obtained from probes
 316 and calibrated by laboratory measurements, while the relative dielectric permittivity of water is
 317 assumed to be 79.5 at a temperature of 22.0 °C (Buchner et al., 1999). The model was divided
 318 into three layers, and the inversion was carried out for each of the layers separately. This step
 319 was done to investigate the effect of geological vertical heterogeneities on the obtained
 320 petrophysical parameters. The model discretization and layering were designed according to
 321 the geological characteristics and hydrogeological simulations results (see section 5.3.1).



322

323 **Fig. 2.** The inversion algorithm workflow which was done for the Archie and CRIM models
 324 separately. The inversion procedure is based on finding the combinations of petrophysical
 325 parameters that can provide the best fit between the measured geophysical data and the
 326 geophysical profiles calculated by using the water content profiles simulated by HYDRUS-1D.

327 The results analysis is based on obtaining the combined values of the varied Archie (a and m)
 328 and CRIM parameters (α and ϵ_s) that have the minimal observed RMSE while the algorithm
 329 fits the calculated and the measured data. The ranges of variability set for each of the parameters
 330 during the inversion were based on common ranges provided in literature for limestone
 331 formations. However, the parameters were set to also have values outside these ranges to avoid
 332 directing the inversion towards literature values, and to compare our results with those reported
 333 in previous studies. Table 1 shows the ranges of the Archie and CRIM parameters used for this
 334 inversion and those most commonly reported in the literature for limestone formations. To
 335 improve the inversion performance and reduce the different parameters dependencies, the
 336 saturation exponent n was fixed to a value of 2 and the calculation was done only for the a and
 337 m parameters in the Archie equation. Even though values ranging between 1.4 and 2.5 have
 338 been previously given to n in the literature for rocks (e.g., Schön, 2004; Sweeney and Jennings,

1960; Rust, 1952), in practice, the saturation exponent is commonly set to 2 for most types of rocks in the absence of laboratory measurements (e.g. Yaramanci et al., 2000; Looms et al., 2008a, 2008b). On the other hand, α was given a range based on its extreme values which are 1 and -1. The lower boundary (-1) represents the harmonic arrangement of dielectric components in series, while its upper boundary (1) represents the arithmetic arrangement of dielectric components in parallel (Chan and Knight, 2001;1999).

Table 2 : The ranges of the Archie (a, m and n) and CRIM (α and ϵ_s) parameters used for the inversion and those commonly reported in the literature for limestone formations.

Model	Parameter	Literature (limestone)	Inversion
Archie	a	$0.2 \leq a \leq 2.3$	$0.1 \leq a \leq 10$
	m	$1.6 \leq m \leq 3$	$1.0 \leq m \leq 10$
	n	$1.5 \leq n \leq 2.5$	n = 2
CRIM	α	$-1 \leq \alpha \leq 1$	$-1 \leq \alpha \leq 1$
	ϵ_s	$4 \leq \epsilon_s \leq 11$	$1 \leq \epsilon_s \leq 20$

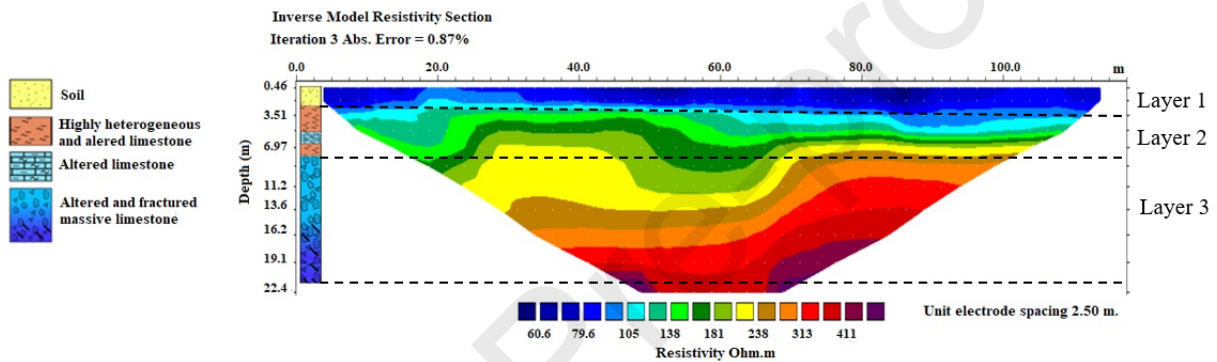
5. Results and discussion

5.1. Geology

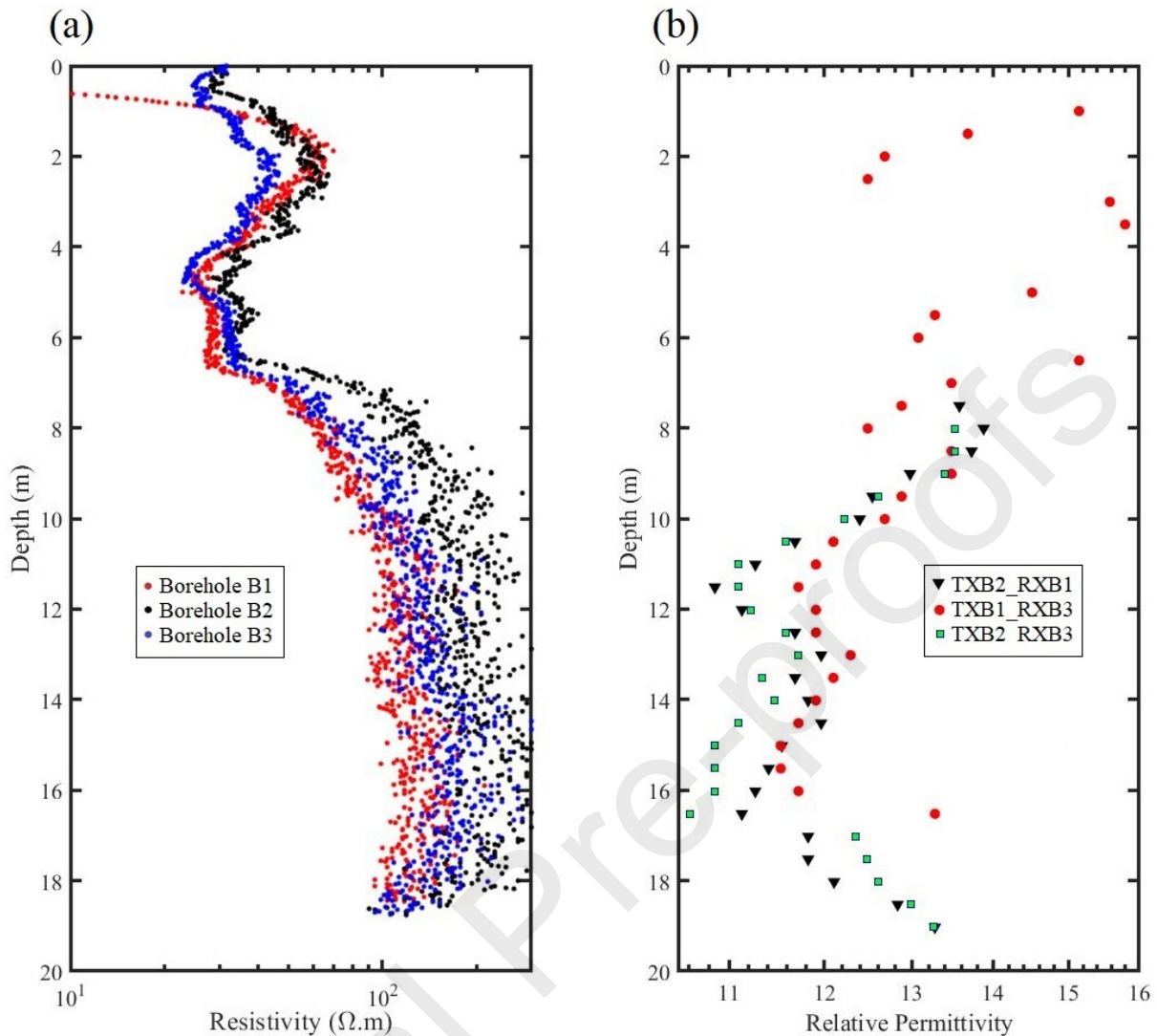
Knowing that a strong coherence was observed between the ERT and borehole ER profiles, throughout this work, the ERT profiles are only used for the lithological description and 2-D representation, while the borehole ER data will be used for the water content analysis and as an input in the inversion for its higher resolution (2 cm) and larger number of data points.

In correspondence with the geological description, the ERT (profile P2 in Fig. 1) showed three main layers corresponding to the three main geological units shown in Fig. 1 (Fig. 3). The data showed a first low ER unit representing the top soil layer. The latter is followed by a moderate

356 ER layer down to a depth of around 7 m. This layer corresponds to the incoherent and altered
 357 limestone formation. Lateral ER variations (Fig. 3) and dispersed dielectric permittivity values
 358 (Fig. 4b) were observed in this layer, which reflects the heterogeneity of this formation. A clear
 359 transition zone between the incoherent limestone layer and the underlying hard limestone rock
 360 layer is evident in the relative permittivity and ER data at depths between 6.5 m and 9 m. This
 361 is followed by a third relatively higher ER layer corresponding to the massive limestone rock
 362 layer. This layer shows lower dielectric permittivity values which started to increase again as
 363 the measurements got closer to the water table level (Fig. 4b).



364
 365 **Fig. 3.** The 2D smoothness-constrained distribution of electrical resistivity of profile P2.
 366 showing 3 main units in accordance with the geology data presented in Fig. 1. All the ERT
 367 profiles showed similar results in terms of the lithological structure, therefore, only profile P2
 368 is presented in this work.

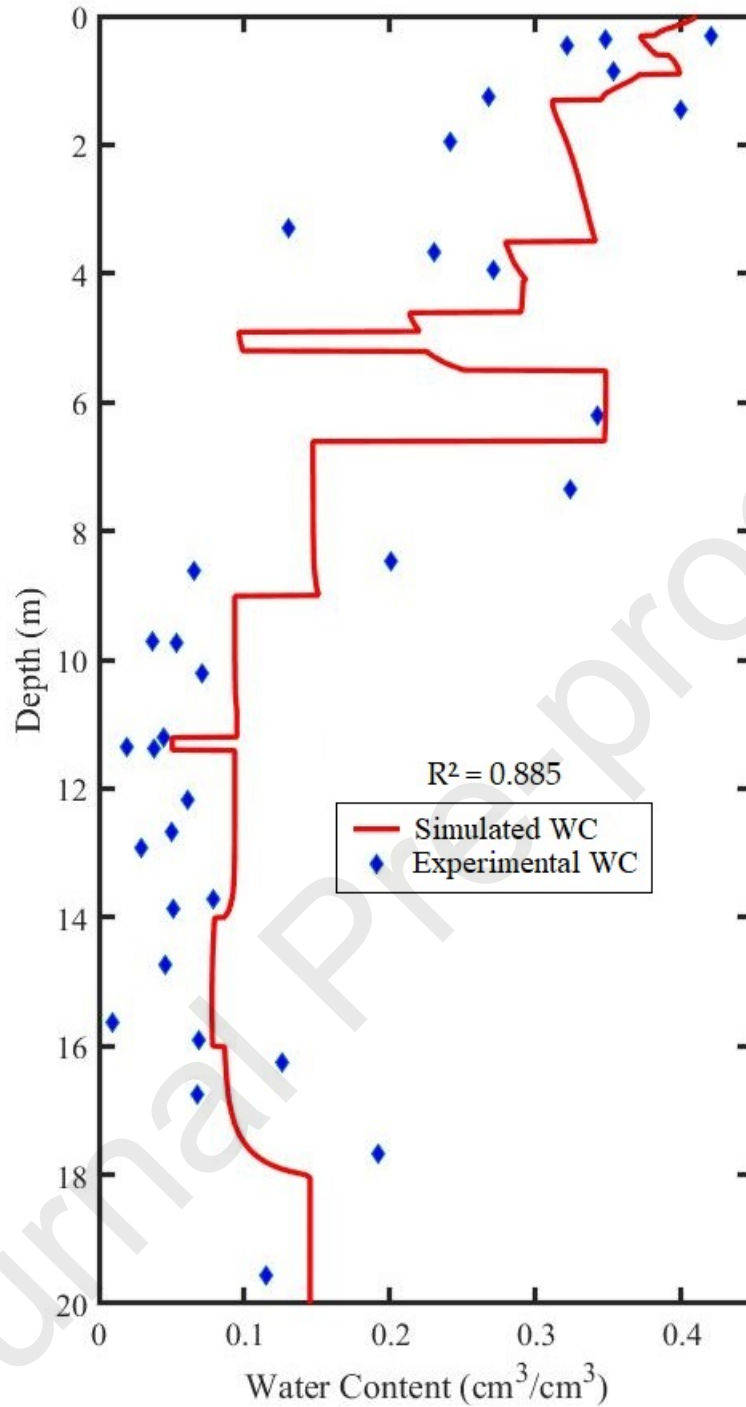


369

370 **Fig. 4.** (a) Electrical resistivity borehole data showing the ER variations in boreholes B1, B2
 371 and B3 (23/03/2017). (b) Relative permittivity results obtained from the cross-hole GPR
 372 profiles acquired between boreholes B1, B2 and B3 (24/01/2019).

373 5.2. Hydrogeology

374 As shown in Fig. 5, the simulated water content profile obtained by the model for borehole B2
 375 (23/03/2017) showed a good agreement with experimental water content ($R^2 > 0.885$) measured
 376 at the same date. This model, which focused on the simulation of the water movement within
 377 the matrix components of the VZ, seemed to constitute a first simplified but suitable approach
 378 for the unidimensional simulation of water flow within the VZ of the Beauce limestone aquifer.



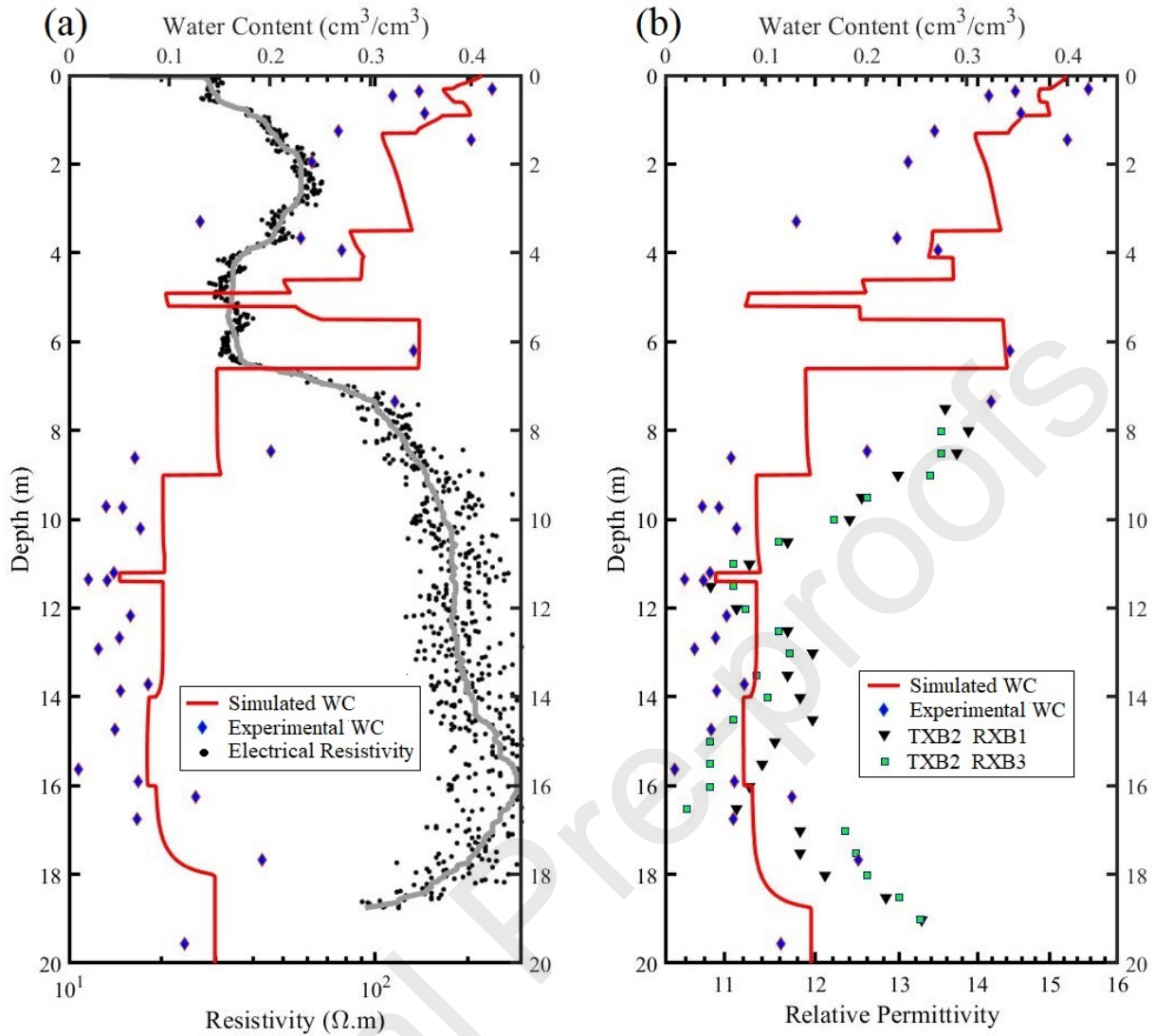
379

380 **Fig. 5** : Experimental water content (WC) plotted against the simulated water content obtained
 381 in borehole B2 with the HYDRUS-1D software (23/03/2017).

382 The borehole ER data (23/03/2017) showed a good global correspondence with the simulated
 383 water content distribution at the same date (Fig. 6a). This correspondence is characterized with
 384 a global increase in the ER values along with the global decrease in the water content. This was

385 followed by a decrease in the ER values with the increase in the water content close to the water
386 table level. Similarly, the relative permittivity data showed a good correspondence with the
387 water content variations (Fig. 6b). A significant coherent decrease in the relative permittivity
388 and water content was observed at a depth between 6.5 m and 9 m located at the transition zone
389 between the incoherent limestone and the hard limestone formations. This was followed by a
390 significant increase in the relative dielectric permittivity values along with the increase in water
391 content close to the water table level. The water content profiles simulated for the dates of the
392 ER (Fig. 6a) and GPR (Fig. 6b) data showed similar values with slight but noticeable
393 differences in the top 6 meters and at a depth between 17 m and 19 m. This was expected
394 knowing that these profiles were simulated for two close periods of the year (23rd of March and
395 24th of January).

396 A similar pattern was observed in the three boreholes ER data and in the three dielectric
397 permittivity profiles, which shows a good repeatability of the field geophysical data. This
398 observation also indicates that the zones around and between the boreholes are globally and
399 relatively homogeneous, despite the presence of local lateral heterogeneities that were observed
400 in each of the geophysical profiles.



401

402 **Fig. 6.** (a) Borehole ER variations with respect to water content variations simulated by
 403 HYDRUS-1D (B2, 23/03/2017), (b) Relative dielectric permittivity distribution obtained from
 404 the GPR measurements with respect to water content variations simulated by HYDRUS-1D
 405 (B2, 24/01/2019). The water table in borehole B2 had a depth of 18.71 m during the ER
 406 measurements and a depth of 18.98 m during the GPR measurements.

407 5.3. Determination of Petrophysical Parameters

408 To determine the Archie (a and m) and CRIM (α and ϵ_s) petrophysical parameters, the measured
 409 ER and relative permittivity data and the simulated water content distributions were used in the
 410 inversion algorithm described in section 4.3.

411 5.3.1. Model Structure

412 As explained previously in section 4.2, the calculation was done for the part of the VZ located
413 at a depth between 6.61 m and 19 m, where the well-cemented microcrystalline texture of the
414 hard limestone rock along with its very low amount of fine-grained material (Aldana et al.,
415 2021) permits the neglect of the grains surface conductivity. Therefore, the inversion model
416 was applied on the geological unit number 3 (Table 1), which was divided into three sub-layers
417 according to lithological description, the hydrogeological model discretization and the water
418 content variations. Layer 1 is located at the top of the unit at a depth between 6.61 m and 9.00
419 m. This layer, which is considered as the transition zone between the incoherent limestone (P_D)
420 and the massive rock (R_B) materials (Table 1), showed simulated water content variations
421 ranging between 0.147 and 0.151 cm^3/cm^3 (Fig. 5). Layer 2 is located at a depth ranging
422 between 9.01 m and 14.00 m, and is characterized by a limestone rock showing few fissures
423 and slight alterations (R_D) with intercalations of massive limestone rock banks (R_C) (Mallet et
424 al., 2022) which presented a very low porosity (Table 1). Layer 2 showed a simulated water
425 content variation ranging between 0.050 and 0.095 cm^3/cm^3 . Layer 3 corresponds to the altered
426 limestone rock that showed a highly heterogeneous structure characterized by an increased
427 evolution towards fracturation and karstification with depth. Layer 3 is located at a depth
428 ranging between 14.01 m and 19 m, and showed the highest water content variation with values
429 ranging between 0.078 and 0.145 cm^3/cm^3 . The simulated water content values described here
430 are those obtained for the ER measurements date (23/03/2017), while similar value ranges were
431 also obtained for those of the GPR measurements date (24/01/2019). The inversion was carried
432 out for each of the model's layers separately in order to investigate the effects of vertical
433 heterogeneities on the obtained parameters. This gives us a total of 6 inversions (3 for the CRIM
434 and 3 for the Archie's model).

435 5.3.2. Inversion Results

436 The inversion results of the Archie's parameters showed a value of 1.60 for the cementation
437 exponent m in Layers 1 and 2 and a value of 1.47 in Layer 3. One can look at the cementation
438 exponent as a measure of connectedness of the pore network which decreases as the m exponent
439 increases (Glover, 2017). Most sediments or sedimentary rock consisting partially or
440 completely of sand-sized fragments have cementation exponents ranging between 1.5 and 2.5
441 (Glover et al., 1997), while lower connectedness and vuggy limestone formations are expected
442 to be represented by higher m values. A wide range of values have been reported in the literature
443 for limestone formations (Worthington, 1993). Values ranging between 1.6 and 2.4 have been
444 reported for carbonates (Schön, 2004; Carothers, 1968; Hill and Milburn, 1956), while it was
445 also suggested that they can also have higher values ranging between 2.5 and 5 due to their
446 poorly connected pore space (Tiab and Donaldson, 2011, 2004). However, knowing that
447 connectedness is a term which also describes the extent to which transport pathways are
448 available, low porosity rocks characterized by relatively direct flow paths due to a well-
449 developed fracture network could have lower values or values close to unity reflecting a fairly
450 good connectedness provided by the fractures network. Therefore, the relatively low values
451 obtained in our study could be related to a well-developed fracture network which is thought to
452 be present in the study site but not fully characterized yet. Even though we used a simple
453 porosity model that doesn't take fractures network into account in the porosity parameter, the
454 relative effect of the fracturation could be reflected in the field resistivity data that have a major
455 influence on the obtained m value during the inversion. Layer 3, which showed a lower m value
456 (1.47) relative to Layers 1 and 2, has a highly heterogeneous structure characterized by
457 increased alteration, fracturation and karstification features relative to the other layers, which
458 might explain the relative decrease of m in this layer. Indeed, complex structural formations
459 have been observed in the limestone VZ at the O-ZNS site (Fig. 7), where fissures, fractures
460 and karst networks were observed at the field scale (Aldana et al., 2021). For example,

461 millimetric vugs induced by dissolution processes have been observed in the weathered rock
 462 formations located at the water table fluctuation zone and corresponding to Layer 3. Further
 463 dissolution episodes could have increased the vugs diameters and enhanced the permeability at
 464 this layer. As it is evident in the Archie's equation (Eq. 7), the higher is the cementation
 465 exponent the higher is the sensitivity of the electrical resistivity values to changes in porosity
 466 (Ellis and Singer, 2007). The relatively similar m values that were obtained in the three layers
 467 indicate a similar sensitivity of the electrical resistivity values to the slight differences in
 468 porosity observed in the different layers.



469
 470 **Fig. 7.** Images of the altered and fissured limestone formation taken while drilling the main
 471 well at the O-ZNS observatory.

472 **Table 3.** The Archie's petrophysical parameters obtained in the three layers of the model.

Layer	Depth (m)	a	m	n
1	6.61-9.00	0.80	1.60	2.00
2	9.01-14.00	0.70	1.60	2.00
3	14.01-19.00	0.60	1.47	2.00

473
 474 The inversion results showed a value of 0.8 for the parameter a in layer 1, while it showed a
 475 value of 0.7 and 0.6 in layers 2 and 3 respectively. Even though no real correlation was found
 476 between this parameter and tortuosity or lithology, a is an empirical constant which is believed
 477 to have a role in the compensation for systematic errors in the porosity, electrical resistivity or
 478 pore fluid resistivity measurements (Glover, 2016, 2015). This empirical factor which appeared

479 in the Winsauer et al. (1952) modification of the Archie's first law usually provided improved
480 fits with experimental data, especially when dealing with low-quality and sparse types of
481 datasets. It is commonly assumed that the size of a is a measure of the extent to which an overall
482 systematic error is present in the measurements. Recent research suggested that these errors
483 produce non-unity values of a , while the closer this parameter is to unity, the better is the data
484 quality. Additionally, a has an important role in the calculation of a more accurate m value,
485 since it compensates for the experimental errors present in the parameters used to calculate m
486 during the fitting procedure (Glover, 2016). Throughout the inversion, a takes the appropriate
487 fitted value to compensate for the presence of systematic errors and reduce their effects on the
488 obtained m value. Therefore, the value of a obtained from the fit can be considered as an
489 empirical parameter that describes the accuracy of the measured data in the Archie equation.
490 The observed decreasing behavior value of a , from 0.8 in layer 1 to 0.6 in layer 3 could be
491 attributed to the increase in the measurements errors associated with the evolution of alteration,
492 fracturation and karstification with depth. This phenomenon can increase the medium
493 heterogeneities and produce errors in the field measurements which the fitted value of a
494 compensated for during the inversion. Even though a was not shown to have an underlying
495 physical meaning, few studies suggested a values ranging between 0.4 and 2.3 in the case of
496 limestone formations (Timur et al., 1972; Porter and Carothers, 1970; Carothers, 1968). In
497 accordance with our inversion results, the most recent studies reported values of a ranging
498 between 0.2 and 1.8 for limestone formations (Glover, 2016, 2015).

499 The inversion of the CRIM showed a ϵ_s value of 7.99 in Layer 1, 7.97 in Layer 2 and 8.00 in
500 Layer 3. ϵ_s is mainly influenced by the mineralogy and rock formation characteristics.
501 Therefore, similar values were expected to be observed in the three layers, knowing that they
502 are all considered as part of the limestone rock main geological unit (Table 1). However, the
503 slight differences in the ϵ_s values observed in the three layers can be attributed to the differences

504 in the geological characteristics of the layers in terms of materials heterogeneity and degree of
 505 alteration which evolved with depth. Nevertheless, these slight differences, as small as they are,
 506 could also be simply induced by the mathematical procedure of the inversion. In accordance
 507 with our results, values ranging between 4 and 13 have been reported in the literature for the
 508 solid phase dielectric permittivity of limestone formations, which is considered as one of the
 509 main sources of uncertainties in the electromagnetic waves application of the CRIM model
 510 (Mount and Comas, 2014; Reynolds, 2011; Cassidy, 2009).

511 The inversion of the CRIM showed an α value of 0.50 in Layer 1, 0.58 in Layer 2 and 0.61 in
 512 Layer 3. Values ranging between -1 and 1 were reported for α over the last few decades, which
 513 is a geometrical factor connecting the effective layering direction of the components to the
 514 applied electric field direction (West et al., 2003; Knoll, 1996; Roth et al., 1990). Several GPR
 515 studies indicated that most geological facies can take an α value of 0.5 (West et al., 2003; Knoll,
 516 1996). Values ranging between 0.46 and 0.65 have been previously obtained during laboratory
 517 measurements (Mount and Comas, 2014; Moysey and knight, 2004).

518 **Table 4.** The CRIM's petrophysical parameters obtained in the model layers.

Layer	Depth (m)	α	ϵ_s
1	6.61-9.00	0.50	7.99
2	9.01-14.00	0.58	7.97
3	14.01-19.00	0.61	8.00

519 This approach was shown to produce acceptable results reflected in a very good fit between the
 520 measured and calculated data in the three layers, and with values that generally fall in the ranges
 521 reported in previous studies. The degree of accuracy of this approach is defined by the
 522 resolution of the hydrogeological model and its capability in capturing the VZ water content
 523 variations. The water content distribution is strongly influenced by the extent of heterogeneities
 524 incorporated in the hydrogeological model and in the porosity parameter of the empirical

relationships, especially in limestone formations with complex porosity patterns. Characterizing the impact of the observed fissures and fractures networks on the water flow at the field scale of the O-ZNS VZ is indeed crucial. Therefore, our future work is focused on the development of a precise description of the water flow through the whole porosity of this highly heterogeneous VZ by combining 3D experimental observations and numerical simulations with dual-porosity or dual-permeability approaches. This will form the basis to incorporate the complex multiple porosity patterns in the petrophysical relationships in order to provide an improved estimation of petrophysical parameters. The geological heterogeneities encountered at different study sites might explain the wide range of values reported in the literature for the Archie's and CRIM's parameters, especially in carbonate geology environments, which are complex mediums that can develop different porosity patterns, fractures networks and flow paths.

6. Conclusion

This study attempted to investigate the relationship between geophysical properties and water content distribution, and determine the Archie's and CRIM's petrophysical parameters by integrating ER and dielectric permittivity data with simulated water content data at the scale of a highly heterogeneous limestone VZ. The simulated and experimental hydrogeological data displayed a very good correspondence with the geophysical data reflected in coherent variations in water content, ER and relative permittivity. These observations showed a significant sensibility of geophysical methods to water content variations, and demonstrated the potential of these methods in investigating hydrogeological processes at our study site.

The inversion results of the Archie model showed values ranging between 0.6 and 0.8 for a and between 1.47 and 1.60 for m . On the other hand, the inversion results of the CRIM showed values ranging between 0.50 and 0.61 for α and between 7.97 and 8.00 for ϵ_s . Similar results

549 were obtained in the three model layers, with slight differences that were attributed to the
550 vertical heterogeneities of the limestone rock formation (e.g., degree of alteration, fracturation,
551 karstification). This observation demonstrates the sensitivity of petrophysical parameters to
552 vertical geological heterogeneities that should be taken into account when calculating these
553 parameters. Given the ranges of variability used in the inversion, the obtained values are within
554 the bounds of values found in the literature, where a wide range have been reported for
555 carbonate formations due to their complex geological features that might vary greatly among
556 different study sites.

557 Throughout this study, the petrophysical parameters were successfully obtained with a very
558 good fit between the measured and simulated data. However, the demonstrated approach
559 showed an important sensitivity to the resolution of water content variations captured by the
560 used hydrogeological model, and to the geological heterogeneities of the medium. Therefore,
561 the perspectives include further improvements to this approach by conducting extensive studies
562 at larger scales, and combining 3D experimental observations and numerical simulations using
563 dual-porosity and dual-permeability modeling approaches that can capture the water content
564 and geological heterogeneities at a higher resolution in complex and fractured limestone
565 formations. In this context, our future work is focused on the development of a geological model
566 constrained by laboratory calibrations that can give a better estimation of the limestone complex
567 porosity patterns to be incorporated in the hydrogeological model and empirical relationships.

568 **Acknowledgment**

569 This study was conducted within the framework of the O-ZNS project which is part of the
570 PIVOTS program (<https://plateformes-pivots.eu/o-zns/?lang=en>). We gratefully acknowledge
571 the financial support provided to the PIVOTS project by the Région Centre–Val de Loire (ARD
572 2020 program and CPER 2015-2020), and by the French Ministry of Higher Education and

573 Research. This research work is co-funded by the Labex Voltaire (ANR-10-LABX-100-01) and
574 by the European Union with the European Regional Development Fund (FEDER) in Centre-
575 Val de Loire. Data can be obtained upon request to the corresponding author. In addition, the
576 data will be soon available on an O-ZNS data repository with their own DOI.

577 **References**

- 578 Abbar, B., Isch, A., Michel, K., Abbas, M., Vincent, H., Abbasimaedeh, P., & Azaroual, M.
579 (2021). Fiber optic technology for environmental monitoring: state of the art and
580 application in the observatory of transfers in the vadose zone (O-ZNS). Chapter book in
581 “Instrumentation and Measurement Technologies for Water Cycle Management”,
582 Springer (Wiley). <https://link.springer.com/book/9783031082610>.
- 583 Abbas, M., Jardani, A., Soueid Ahmed, A., Revil, A., Brigaud, L., Bégassat, Ph., & Dupon, J.
584 P. (2017). Redox potential distribution of an organic-rich contaminated site obtained by
585 the inversion of self-potential data. *Journal of Hydrology*. 554,111–127.
586 <https://doi.org/10.1016/j.jhydrol.2017.08.053>.
- 587 Ahmed, A. S., Jardani, A., Revil, A., & Dupont, J. P. (2014). Hydraulic conductivity field
588 characterization from the joint inversion of hydraulic heads and self-potential data.
589 *Water Resources Research* . 50, 3502–3522. <https://doi.org/10.1002/2013WR014645>.
- 590 Aldana, C., Isch, A., Bruand, A., Azaroual, M., & Coquet., Y. (2021). Relationship between
591 hydraulic properties and material features in a heterogeneous vadose zone of a
592 vulnerable limestone aquifer. *Vadose Zone Journal*. e20127.
593 <https://doi.org/10.1002/vadosezonej2.20127>.
- 594 Ammar, A. & Kamal, K. A. (2017). Resistivity method contribution in determining of fault
595 zone and hydro-geophysical characteristics of carbonate aquifer, eastern desert, Egypt.
596 *Applied Water Science*. <https://doi.org/10.1007/s13201-017-0639-9>.
- 597 Archie, G. E. (1942). The electrical resistivity log as an aid in determining some reservoir
598 characteristics. *Transactions of American Institute of Mining Metallurgical Engineers*.
599 146. 54-62. <https://doi.org/10.2118/942054-G>.

- 600 Arora, B., Dwivedi, D., Faybishenko, B., Jana, R., & Wainwright, H. (2019). Understanding
601 and Predicting Vadose Zone Processes. *Reviews in Mineralogy*, 85.
602 <https://doi.org/10.1515/9781501512001-011>.
- 603 Birchak, J. R., Gardner, C. G., Hipp, J. E., & Victor, J. M. (1974). High dielectric constant
604 microwave probes for sensing soil moisture. *IEEE*, 62: 93-98. doi:
605 10.1109/PROC.1974.9388.
- 606 Binley, A., Winship, P., Middleton, R., Pokar, M., & West, J. (2001). High-resolution
607 characterization of vadose zone dynamics using crossborehole radar. *Water Resources*
608 *Research*. 37(11), 2639–2652. <https://doi.org/10.1029/2000WR000089>.
- 609 Binley, A., Cassiani, G., Middleton, R., & Winship, P. (2002a). Vadose zone flow model
610 parameterisation using cross-borehole radar and resistivity imaging. *Journal of*
611 *Hydrology*. 267:147–159. [https://doi.org/10.1016/S0022-1694\(02\)00146-4](https://doi.org/10.1016/S0022-1694(02)00146-4).
- 612 Binley, A., Cassiani, G., & Deiana, R. (2010). Hydrogeophysics - Opportunities and
613 Challenges. *Bollettino di Geofisica Teorica ed Applicata*, 51. 267-284.
- 614 Binley, A., Hubbard, S. S., Huisman, J. A., Revil, A., Robinson, D. A., Singha, K., & Slater, L.
615 D. (2015). The emergence of hydrogeophysics for improved understanding of
616 subsurface processes over multiple scales. *Water Resources Research*. 51. 3837–3866.
617 <https://doi.org/10.1002/2015WR017016>.
- 618 Blazevic, L., Bodet, L., Pasquet, S., Linde, N., Jougnot, D., Longuevergne, L. (2020). Time-
619 Lapse Seismic and Electrical Monitoring of the Vadose Zone during A Controlled
620 Infiltration Experiment at the Ploemur Hydrological Observatory, France. *Water*. 12.
621 10.3390/w12051230.
- 622 Brunet, P., Clément, R., & Bouvier, C. (2010). Monitoring soil water content and deficit using
623 Electrical Resistivity Tomography (ERT) – A case study in the Cevennes area, France.
624 *Journal of Hydrology*, 380. 146-153. <https://doi.org/10.1016/j.jhydrol.2009.10.032>.
- 625 Buchner, R., Barthel, J., & Stauber, J. (1999). The dielectric relaxation of water between 0°C
626 and 35°C. *Chemical Physics Letters*. 306(1–2), 57– 63. [https://doi.org/10.1016/S0009-](https://doi.org/10.1016/S0009-2614(99)00455-8)
627 [2614\(99\)00455-8](https://doi.org/10.1016/S0009-2614(99)00455-8).
- 628 Carothers, J. E. (1968). A statistical study of the formation factor relation. *The Log Analyst* 9
629 (5). 13-20 .

- 630 Cassiani, G., Ferraris, S., Giustiniani, M., Deiana, R., & Strobba, C. (2009b). Time-lapse
631 surface-to-surface GPR measurements to monitor a controlled infiltration experiment.
632 *Bollettino di Geofisica Teorica ed Applicata*. 50. 209-226.
- 633 Cassidy, N. (2009). *Ground Penetrating Radar Data Processing, Modelling and Analysis*.
634 <https://doi.org/10.1016/B978-0-444-53348-7.00005-3>.
- 635 Chan, C. Y., & Knight; R. J. (2001). Laboratory measurements of electromagnetic wave
636 velocity in layered sands, *Water Resources Research*, 37(4), 1099–1105,
637 doi:10.1029/2000WR900356.
- 638 Chan, C. Y., & Knight; R. J. (1999). Determining water content and saturation from dielectric
639 measurements in layered materials. *Water Resources Research*. 35. 85-93.
640 doi/pdf/10.1029/1998WR900039.
- 641 Dafflon, B., Irving, J., & Barrash, W. (2011). Inversion of multiple intersecting high-resolution
642 crosshole GPR profiles for hydrological characterization at the Boise hydrogeophysical
643 research site. *Journal of Applied Geophysics*. 73:305–314.
644 <https://doi.org/10.1016/j.jappgeo.2011.02.001>.
- 645 De Jong, S., Heijenk, R., Nijland, W., & Meijde, M. (2020). Monitoring Soil Moisture
646 Dynamics Using Electrical Resistivity Tomography under Homogeneous Field
647 Conditions. *Sensors (Basel, Switzerland)*. 20(18). 5313. [https://doi.org/ 20.](https://doi.org/10.3390/s20185313)
648 [10.3390/s20185313](https://doi.org/10.3390/s20185313).
- 649 Eching, S. O., Hopmans, J. W., & Wendroth, O. (1994). Unsaturated hydraulic conductivity
650 from transient multistep outflow and soil water pressure data. *Soil science society of*
651 *America journal* 58(3): 687–695.
- 652 Ellis, D. V., & Singer, J. M. (2007). *Well Logging for Earth Scientists*. Vol. 692, Springer,
653 Dordrecht.
- 654 Evett, S. (2003). *Soil Water Measurement by Time Domain Reflectometry*. In *Encyclopedia of*
655 *Water Science*; Marcel Dekker, Inc.: New York, NY, USA; ISBN 0-8247-4241-9.
- 656 Evett, S. (2008). Neutron moisture meters. *Field Estimation of Soil Water Content: A Practical*
657 *Guide to Methods, Instrumentation, and Sensor Technology*. 39-54. ISSN 1018–5518.
- 658 Gardner, W. R. (1956). Calculation of Capillary Conductivity from Pressure Plate Outflow
659 Data. 317–320p.

- 660 Garré, S., Hyndman, D., Mary, B., and Werban, U. (2021). Geophysics conquering new
661 territories: The rise of Agrogeophysics. *Vadose Zone Journal*. p. e20115.
662 <https://doi.org/10.1002/vzj2.20115>.
- 663 Gance, J., Malet, J. P., Supper, R., Sailhac, P., Ottowitz, D., & Jochum, B. (2016). Permanent
664 electrical resistivity measurements for monitoring water circulation in clayey landslides.
665 *Journal of Applied Geophysics*. 126, 28-115.
666 <https://doi.org/10.1016/j.jappgeo.2016.01.011>.
- 667 Glover, P. W. J., Gomez, J. B., Meredith, P. G., Hayashi, K., Sammonds, P. R., & Murrell, S.
668 A. F. (1997). Damage of saturated rocks undergoing triaxial deformation using complex
669 electrical conductivity measurements: experimental results: *Physics and Chemistry of*
670 *the Earth*, 22, no. 1–2, 57–61. doi: 10.1016/S0079-19469700078-5.
- 671 Glover, P. W. J. (2009). What is the cementation exponent? A new interpretation. *The Leading*
672 *Edge*, 28, 82–85. <https://doi.org/10.1190/1.3064150>.
- 673 Glover, P. W. J. (2010). A generalised Archie's law for n phases. *Geophysics*. 75, E247–E265.
674 <https://doi.org/10.1190/1.3509781>, 2010.
- 675 Glover, P. W. J. (2015). Geophysical properties of the near surface Earth: Electrical properties.
676 *Treatise on Geophysics*, 11, 89–137, 2015. [https://doi.org/10.1016/B978-0-444-53802-](https://doi.org/10.1016/B978-0-444-53802-4.00189-5)
677 [4.00189-5](https://doi.org/10.1016/B978-0-444-53802-4.00189-5).
- 678 Glover, P. (2016). Archie's law – a reappraisal: *Solid Earth*. 7. 1157-1169.
679 <https://doi.org/10.5194/se-7-1157-2016>.
- 680 Glover, P. W. J. (2017). A new theoretical interpretation of Archie's saturation exponent. *Solid*
681 *Earth*. 8. 805-816. <https://doi.org/10.5194/se-8-805-2017>.
- 682 Griffiths, D. H., Barker, R. D. (1993). Two-dimensional resistivity imaging and modeling in
683 areas of complex geology. *Journal of Applied Geophysics*. 29. 211–226.
- 684 Hagrey, S. (2007). Geophysical imaging of root-zone, trunk, and moisture heterogeneity.
685 *Journal of experimental botany*. 58. 839-54. <https://doi.org/10.1093/jxb/erl237>.
- 686 He, H., Aogu, K., Li, M., Xu, J., Sheng, W., Jones, S.B., González-Teruel, J.D., Robinson,
687 D.A., Horton, R., Bristow, K., Dyck, M., Filipović, V., Noborio, K., Wu, Q., Jin, H.,
688 Feng, H., Si, B., & Lv, J. (2021). Chapter Three - A review of time domain reflectometry

- 689 (TDR) applications in porous media. In: D.L. Sparks (Ed.). *Advances in Agronomy*.
690 Academic Press. 83-155. <https://doi.org/10.1016/bs.agron.2021.02.003>.
- 691 Hendrickx, J. M. H., Das, B., Corwin, D. L., Wraith, J. M., & Kachanoski, R. G. (2002).
692 Relationship between soil water solute concentration and apparent soil electrical
693 conductivity. In Dane, J. H., Topp, G.C. (Eds.), *Methods of Soil Analysis: Part 4.*
694 *Physical Methods*. Soil Science Society of America, Madison, WI, USA. 1275–1282.
- 695 Herkelrath, W. N., Hamburg, S. P., & Murphy, F. (1991). Auto- matic, real-time monitoring of
696 soil moisture in a remote field area with time domain re- flectometry. *Water Resources*
697 *Research*. 27, 857- 864.
- 698 Hill, H. J., & Milburn, J. D. (1956). Effect of clay and water salinity on electrochemical
699 behaviour of reservoir rocks. *Petroleum Transactions*. 207. 65–72.
700 <https://doi.org/10.2118/532-G>.
- 701 Hubbard, S. S., Chen, J. S., Peterson, J., Majer, E. L., Williams, K., Swift, D. J., Mailloux, B.,
702 & Rubin, Y. (2001a). Hydrogeological characterization of the South Oyster Bacterial
703 Transport Site using geophysical data. *Water Resources Research*. 37(10). 2431–2456.
704 <https://doi.org/10.1029/2001WR000279>.
- 705 Huisman, J. A., Hubbard, S. S., Redman, J. D., & Annan, P. A. (2003), Measuring soil water
706 content with ground penetrating radar: A review. *Vadose Zone Journal*. 2(4). 476–491.
707 <https://doi.org/10.2113/2.4.476>.
- 708 Isch, A., Montenach, D., Hammel, F., Ackerer, P., Coquet, Y (2019). A Comparative Study of
709 Water and Bromide Transport in a Bare Loam Soil Using Lysimeters and Field Plots.
710 *Water*. 11. 1199. <https://doi.org/10.3390/w11061199>.
- 711 Isch, A., Coquet, Y., Abbar, B., Aldana, B., Abbas, M., Bruand, A., Azaroual, M. (2022). A
712 comprehensive experimental and numerical analysis of water flow and travel time in a
713 highly heterogeneous vadose zone. *Journal of Hydrology*. 610. 127875.
714 <https://doi.org/10.1016/j.jhydrol.2022.127875>.
- 715 Jardani, A., Revil, A., & Dupont, J. P. (2012). Stochastic joint inversion of hydrogeophysical
716 data for salt tracer test monitoring and hydraulic conductivity imaging. *Advances in*
717 *Water Resources*. 52. 62-77. <https://doi.org/10.1016/j.advwatres.2012.08.005>.
- 718 Johnson, T. C., Versteeg, R. J., Ward, A., Day-Lewis, F. D., & Revil, A. (2010). Improved
719 hydrogeophysical characterization and monitoring through parallel modeling and

- 720 inversion of time-domain resistivity and induced-polarization data. *Geophysics*. 75. 27-
721 41. <https://doi.org/10.1190/1.3475513>.
- 722 Johnson, T., Versteeg, R., Thomle, J., Hammond, G., Chen, X., & Zachara, J. (2015). Four-
723 dimensional electrical conductivity monitoring of stage-driven river water intrusion:
724 Accounting for water table effects using a transient mesh boundary and conditional
725 inversion constraints. *Water Resources Research*. 51. 6177–6196.
726 <https://doi.org/10.1002/2014WR016129>.
- 727 Klotzsche, A., Jonard, F., Looms, M. C., Van Der Kruk, J., & Huisman, J. A. (2018). Measuring
728 soil water content with ground penetrating radar: A decade of progress. *Vadose Zone*
729 *Journal*. 17:180052. <https://doi.org/10.2136/vadosezonej2018.03.0052>.
- 730 Klotzsche, A., L ¨arm, L., Vanderborght, J., Cai, G., Morandage, S., Z ¨orner, M. (2019).
731 Monitoring soil water content using time lapse horizontal borehole GPR data at the field
732 plotscale. *Vadose Zone Journal*. 18. 190044. <https://doi.org/10.2136/vzj2019.05.0044>.
- 733 Klotzsche, A., Van Der Kruk, J., Linde, N., Doetsch, J., & Vereecken, H. (2013). 3-D
734 characterization of high-permeability zones in a gravel aquifer using 2-D crosshole GPR
735 full-waveform inversion and wave guide detection. *Geophysical Journal International*.
736 195:932–944. <https://doi.org/10.1093/gji/ggt275>.
- 737 Kowalsky, M., Finsterle, S., Peterson, J., Hubbard, S., Rubin, Y., Majer, E., Ward, A., & Gee,
738 G. (2005). Estimation of field-scale soil hydraulic and dielectric parameters through
739 joint inversion of GPR and hydrological data. *Water Resources Research*., 41, W11425,
740 <https://doi.org/10.1029/2005WR004237>.
- 741 Linde, N., Binley, A., Tryggvason, A., Pedersen, L. B., & Revil, A. (2006). Improved hydro-
742 geophysical characterization using joint inversion of cross-hole electrical resistance and
743 ground-penetrating radar traveltime data. *Water Resources Research*. 42. W12404.
744 <https://doi.org/10.1029/2006WR005131>.
- 745 Looms, M. C., Binley, A., Jensen, K. H., Nielsen, L., & Hansen, T. M. (2008a). Identifying
746 unsaturated hydraulic parameters using an integrated data fusion approach on cross-
747 borehole geophysical data. *Vadose Zone Journal*. 7. 238–248.
748 <https://doi.org/10.2136/vadosezonej2007.0087>.

- 749 Looms, M. C., Jensen, K. H., Binley, A., & Nielsen, L. (2008b). Monitoring Unsaturated Flow
750 and Transport Using Cross-Borehole Geophysical Methods. *Vadose Zone Journal*. 7.
751 227–237. <https://doi.org/10.2136/vadosezonej2007.0087>.
- 752 Lucia, F. J. (2007). *Carbonate Reservoir Characterization: An Integrated Approach*. Springer.
753 <https://link.springer.com/book/10.1007/978-3-540-72742-2>
- 754 Lunt, I., Hubbard, S. S., & Rubin, Y. (2005). Soil moisture estimation using ground-penetrating
755 radar reflection data. *Journal of Hydrology*. 307. 254–269.
756 <https://doi.org/10.1016/j.jhydrol.2004.10.014>.
- 757 Mallet, C., Isch, A., Laurent, G., Jodry, C., Azaroual, M. (2022). Integrated static and dynamic
758 geophysical and geomechanical data for characterization of transport properties.
759 *International Journal of Rock Mechanics and Mining Sciences*. 153.
760 <https://doi.org/10.1016/j.ijrmms.2022.105050>.
- 761 Mallet, C., Jodry, C., Isch, A., Laurent, G., Deparis, J. & Azaroual, M. (2021). Multi-
762 geophysical field measurements to characterize lithological and hydraulic properties of
763 a multi-scale karstic and fractured limestone vadose zone: Beauce aquifer (O-ZNS).
764 Chapter book in: *Instrumentation and Measurement Technologies for Water Cycle*
765 *Management*, Springer. <https://link.springer.com/book/9783031082610>.
- 766 Mary, B., Peruzzo, L., Boaga, J., Schmutz, M., Wu, Y., Hubbard, S., & Cassiani, G. (2018).
767 Small scale characterization of vine plant root water uptake via 3D electrical resistivity
768 tomography and Mise-à-la-Masse method. *Hydrology and Earth System Sciences*. 22.
769 5427-5444. <https://doi.org/10.5194/hess-22-5427-2018>.
- 770 Mohamed, A., & Hamada, G. (2017). Determination Techniques of Archie's Parameters: a, m
771 and n in Heterogeneous Reservoirs. *Journal of Geophysics and Engineering*. 14.
772 <https://doi.org/10.1088/1742-2140/aa805c>.
- 773 Mount, G. J., & Comas, X. (2014). Estimating porosity and solid dielectric permittivity in the
774 Miami Limestone using high-frequency ground penetrating radar (GPR) measurements
775 at the laboratory scale. *Water Resources Research*. 50, 7590–7605.
776 <https://doi.org/10.1002/2013WR014947>.
- 777 Mualem, Y. (1976.) A new model for predicting the hydraulic conductivity of unsaturated
778 porous media. *Water Resources Research*. 12(3). 513–522.
779 <https://doi.org/10.1029/WR012i003p00513>.

- 780 Moysey, S., & Knight, R. J. (2004). Modeling the field-scale relationship between dielectric
781 constant and water content in heterogeneous systems. *Water Resources Research*.40.
782 W03510, doi:10.1029/2003WR002589.
- 783 Nimmo, J. R. (2005). Unsaturated Zone Flow Processes. *Encyclopedia of Hydrological*
784 *Sciences*, Wiley, Chichester, UK. 2299–2322.
- 785 Knoll, M. D., (1996). A petrophysical basis for Ground-penetrating radar and very early time
786 electromagnetics, electrical properties of sand-clay mixtures. Unpublished Ph.D.
787 dissertation, University of British Columbia, 316 p.
- 788 Paz, C., Alcalá, F. J., Carvalho, J. M., & Ribeiro, L. (2017). Current uses of ground penetrating
789 radar in groundwater-dependent ecosystems research. *Science of The Total*
790 *Environment*., 595. 868–885. <https://doi.org/10.1016/j.scitotenv.2017.03.210>.
- 791 Porter, C. R. & Carothers, J. E. (1970). Formation factor porosity relation derived from well
792 log data, *Trans. SPWLA 11th Ann. Logging Symp.*, 1–19, 1970.
- 793 Reynolds, J. (2011). *An Introduction to Applied and Environmental Geophysics*. Wiley. ISBN:
794 978-0-471-48535-3.
- 795 Richards, L.A., 1931. Capillary conduction of liquids through porous mediums. *J. Appl. Phys.*
796 1, 318–333. <https://doi.org/10.1063/1.1745010>.
- 797 Robinson, D., Jones, S., Wraith, J., Or, D., & Friedman, S. (2003). A review of advances in
798 dielectric and electrical conductivity measurement in soils using time domain
799 reflectometry, *Vadose Zone Journal*. 2. 444–475. <https://doi.org/10.2113/2.4.444>.
- 800 Robinson, D., Binley, A., Crook, N., Day-Lewis, F., Ferré, T., Grauch, V.J.S, Knight, R., Knoll,
801 M., Lakshmi, V., Miller, R., Nyquist, J., Pellerin, L., Singha, K., & Slater, L. (2008).
802 Advancing process-based watershed hydrological research using near-surface
803 geophysics: A vision for, and review of, electrical and magnetic geophysical methods.
804 *Hydrological Processes – Wiley*. 22. 3604–3635. <https://doi.org/10.1002/hyp.6963>.
- 805 Roth, K., Schulin, R., Fluhler, H., & Attinger, W. (1990). Calibration of time domain
806 reflectometry for water content measurement using a composite dielectric approach.
807 *Water Resources Research*. 26. 2267–2273.
808 <https://doi.org/10.1029/WR026i010p02267>.
- 809 Rubin, Y., & Hubbard, S. S. (2005). *Hydrogeophysics*, 523 pp., Springer, N. Y.

- 810 Rust, C. F. (1952). Electrical Resistivity Measurements on Reservoir Rock Samples by the
811 Two-Electrode and Four-Electrode Methods. AIME Transactions, 195. 217-224.
- 812 Schön, J. H. (2004). Physical Properties of Rocks: Fundamentals and Principles of
813 Petrophysics. Edited by: Helbig, K. and Treitel, S., Vol.18, Amsterdam, the
814 Netherlands: Elsevier, ISBN: 008044346X, 2004.
- 815 Šimůnek, J., van Genuchten, M.T., & Šejna, M. (2016). Recent Developments and Applications
816 of the HYDRUS Computer Software Packages. Vadose Zone Journal. 15(7).
817 <https://doi.org/10.2136/vadosezonej2016.04.0033>.
- 818 Skierucha, W., Wilczek, A., Szyplowska, A., Sławiński, C., Lamorski, K., Skierucha, W.,
819 Wilczek, A., Szyplowska, A., Sławiński, C., & Lamorski, K. (2012). A TDR-based soil
820 moisture monitoring system with simultaneous measurement of soil temperature and
821 electrical conductivity. Sensors, 12. 13545–13566. <https://doi.org/10.3390/s121013545>.
- 822 Steelman, C., & Endres, A. (2011). Comparison of Petrophysical Relationships for Soil
823 Moisture Estimation using GPR Ground Waves. Vadose Zone Journal. 10. 270.
824 <https://doi.org/10.2136/vadosezonej2010.0040>.
- 825 Stephens, D. B. (2019). Vadose Zone Hydrology. CRC Press, 347 Pages. ISBN
826 9780367448783.
- 827 Sweeney, S. A. & Jennings, H. Y. (1960). The electrical resistivity of preferentially water-wet
828 and preferentially oil-wet carbonate rock. Producers Monthly. 24 (7). 29-32, 1960.
- 829 Tiab, D., & Donaldson, E. C. (2004). Petrophysics: Theory and Practice of Measuring Reservoir
830 Rock and Fluid Transport Properties: Second Edition. Gulf Professional Publishing –
831 Elsevier. ISBN: 9780080497655
- 832 Timur, A., Hemkins, W. B., & Worthington, A. E. (1972). Porosity and pressure dependence
833 of formation resistivity factor for sandstones. Trans. CWLS 4th Formation Evaluation
834 Symp., 30 pp.
- 835 Topp, G. C., Davis, J. L., & Annan, A. P. (1980). Electromagnetic determination of soil water
836 content: Measurements in coaxial transmission lines. Water Resources Research.
837 16.574–582. <https://doi.org/10.1029/WR016i003p00574>.

- 838 van Genuchten, M. T. (1980). A closed-form equation for predicting the hydraulic conductivity
839 of unsaturated soils. *Soil Science Society of America Journal*. 44(5). 892–898.
840 <https://doi.org/10.2136/sssaj1980.03615995004400050002x>.
- 841 van Genuchten, M. T., Leij, F. J., & Yates, S. R. (1991). The RetC code for quantifying
842 hydraulic functions of unsaturated soils. EPA/600/2-91/065, R.S. 83.
- 843 Verhoef, A., Fernández-Gálvez, J., Diaz-Espejo, A., Main, B.E. & El-Bishti, M. (2006). The
844 diurnal course of soil moisture as measured by various dielectric sensors: Effects of soil
845 temperature and the implications for evaporation estimates. *Journal of Hydrology*. 321.
846 147-162. <https://doi.org/10.1016/j.jhydrol.2005.07.039>.
- 847 Vereecken, H., Binley, A., Cassiani, G., Revil, A., & Titov, K. (2006). *Applied*
848 *Hydrogeophysics*, 383 pp., Springer, Dordrecht, Netherlands.
- 849 Vilhelmsen, T. N., Behroozmand, A. A., Christensen, S. & Nielsen, T. H. (2014). Joint
850 inversion of aquifer test, MRS, and TEM data. *Water Resources Research*. 50. 3956–
851 3975. <https://doi.org/10.1002/2013WR014679>.
- 852 Wehrer, M., & Slater, L. (2015). Characterization of water content dynamics and tracer
853 breakthrough by 3-D electrical resistivity tomography (ERT) under transient
854 unsaturated conditions. *Water Resources Research*. 51.
855 <https://doi.org/10.1002/2014WR016131>.
- 856 West, L. J., Huang, Y., & Handley, K. (2001). Dependence of Sandstone Dielectric Behaviour
857 on Moisture Content and Lithology. *Proceedings of the Symposium on Applications of*
858 *Geophysics to Engineering and Environmental Problems (SAGEEP2001)*,
859 *Environmental and Engineering Geophysical Society, Denver, CO.*
860 <https://doi.org/10.4133/1.2922904>.
- 861 West, L. J., Handley, K., Huang, Y., & Pokar, M. (2003). Radar frequency dielectric dispersion
862 in sandstone: Implications for determination of moisture and clay content. *Water*
863 *Resources Research*, 39.2. <https://doi.org/10.1029/2001WR000923>.
- 864 Winsauer, W. O., Shearin, H. M., Masson, P. H., & Williams, M. (1952). Resistivity of brine-
865 saturated sands in relation to pore geometry. *AAPG Bull.*, 36, 253–277.
866 <https://doi.org/10.1306/3D9343F4-16B1-11D7-8645000102C1865D>.

867 Worthington, P. F. (1993). The uses and abuses of the Archie equations, 1: The formation
 868 factor-porosity relationship. *Journal of Applied Geophysics.*, 30, 215–228.
 869 [https://doi.org/10.1016/0926-9851\(93\)90028-W](https://doi.org/10.1016/0926-9851(93)90028-W).

870 Yaramanci, U. (2000). Geoelectric exploration and monitoring in rock salt for the safety
 871 assessment of underground waste disposal sites. *Journal of Applied Geophysics.*, 44,
 872 181–196.

873

874

875 **Table 5.** (a) Description of the samples considered for the representation of the VZ profile and
 876 the simulation of water flow with HYDRUS-1D: depth, description, saturated water content (θ_s
 877), experimental saturated water content ($\theta_{sExp.}$), hydraulic conductivity (K_s), α , and n .

Geological Unit	Depth (m)	Sample	Description	θ_s (cm ³ /cm ³)	$\theta_{sExp.}$ (cm ³ /cm ³)	K_s (cm/d)	α cm ⁻¹	n (/)
1	0.00-0.30	S _A	Soil	0.4735	0.4864	30.24	0.0242	1.15
	0.31-0.60	S _B	Soil	0.4661	0.4612	53.57	0.0242	1.16
	0.61-0.90	S _C	Soil	0.5002	0.4162	47.52	0.0366	1.16
2	0.91-1.30	P _A	Powdery limestone	0.4511	0.4230	7.31	0.0247	1.17
	1.30-3.50	P _B	Powdery limestone	0.3659	0.3525	0.455	0.0073	1.25
	3.51-4.10	I _A	Calcareous sand	0.3918	0.3775	35.22	0.0715	1.20
	4.11-4.60	P _C	Powdery limestone	0.2969	0.3080	0.143	0.0031	1.22
	4.61-4.90	I _B	Calcareous sand	0.3698	0.4336	285.49	0.1600	1.23
	4.91-5.20	R _A	Altered rock	0.2984	0.3400	5000	0.5156	1.36
	5.21-5.50	I _B	Calcareous sand	0.3698	0.4336	285.49	0.1600	1.23
	5.51-6.60	P _D	Powdery limestone	0.3527	0.3491	0.185	0.0040	1.22
3	6.61-9.00	R _B	Massive rock	0.1547	0.1499	1.32	0.0150	1.16
	9.01-11.20	R _D	Massive rock	0.0949	0.1180	0.402	0.0096	1.17
	11.21-11.40	R _C	Massive rock	0.0504	0.0491	0.0097	0.0014	1.23
	11.41-14.00	R _D	Massive rock	0.0949	0.1180	0.402	0.0096	1.17
	14.01-16.00	R _E	Massive rock	0.1172	0.1333	500	0.1266	1.15

16.01-19.00 R_F Massive rock 0.1452 0.1639 500 0.1371 1.19

878

879

880

881

882

883 **Table 6** : The ranges of the Archie (a, m and n) and CRIM (α and ϵ_s) parameters used for the

884 inversion and those commonly reported in the literature for limestone formations.

Model	Parameter	Literature (limestone)	Inversion
Archie	a	$0.2 \leq a \leq 2.3$	$0.1 \leq a \leq 10$
	m	$1.6 \leq m \leq 3$	$1.0 \leq m \leq 10$
	n	$1.5 \leq n \leq 2.5$	n = 2
CRIM	α	$-1 \leq \alpha \leq 1$	$-1 \leq \alpha \leq 1$
	ϵ_s	$4 \leq \epsilon_s \leq 11$	$1 \leq \epsilon_s \leq 20$

885

886

887

888

889

890

891

892

893

894

895

896

897

898

899

900
901
902
903
904
905
906
907
908
909
910
911
912
913
914
915
916
917
918
919
920
921

Table 7. The Archie's petrophysical parameters obtained in the three layers of the model.

Layer	Depth (m)	a	m	n
1	6.61-9.00	0.80	1.60	2.00
2	9.01-14.00	0.70	1.60	2.00
3	14.01-19.00	0.60	1.47	2.00

922

923

924 **Table 8.** The CRIM's petrophysical parameters obtained in the model layers.

Layer	Depth (m)	α	ϵ_s
1	6.61-9.00	0.50	7.99
2	9.01-14.00	0.58	7.97
3	14.01-19.00	0.61	8.00

925

926

Journal Pre-proofs